Wideband Broadside-Coupled Line Baluns Enabled by Multimaterial Additive Manufacturing

Joe Steele and Dimitra Psychogiou, *Senior Member, IEEE*

***Abstract*— The manuscript reports on a comprehensive design methodology for the realization of wideband Marchand baluns (MBs) alongside a unique integration concept using multimaterial inkjet printing. An optimization method determining the maximum achievable fractional bandwidth (FBW) is proposed for the first time. Several transmission line (TL)-based integration concepts are analyzed using 2-D and 3-D electromagnetic (EM) simulations to maximize FBW, while considering the process capabilities of a multimaterial, multilayer inkjet printing process which is used in this work for the realization of MBs for first time. A miniaturization scheme using spiral TLs and slanted vias is also explored for size compactness. To validate this approach, several coupled-line test structures and MBs were designed, manufactured, and tested in resistively terminated and back-to-back configurations. They include: 1) a straight MB with a footprint of 0.033 × 0.241 × 0.028 λ_g^3, center frequency (f_0) 4.4 GHz, and 10 dB return loss bandwidth (BW) between 2.8 and 8 GHz (i.e., FBW of 96%). Across this BW, the power loss, phase imbalance (PI), and amplitude imbalance (AI) were measured as 1.2–3.9 dB, 3.5 ± 3.5°, and 0.6 ± 0.3 dB, respectively, and 2) spiral MB with a footprint of 0.043 × 0.094 × 0.028 λ_g^3, f_0 = 4.4 GHz, and BW between 2.35 and 6.8 GHz (i.e., FBW of 95%). The power loss, PI, and AI were measured as 0.9–3.1 dB, 5 ± 2°, and 0.4 ± 0.4 dB, respectively.**

***Index Terms*— Additively manufactured electronics, broadside-coupled lines, Marchand balun (MB), inkjet printing.**

I. Introduction

BALUNS are impedance transformers that interface balanced and unbalanced transmission lines (TLs) and facilitate impedance matching. They are commonly used in balanced antenna feeds [1], mixers [2], differential amplifiers [3], frequency multipliers [4], and phase detectors [5]. As the need for multifunctional RF front-ends capable of supporting many applications and wider operational bandwidths (BWs) increases, RF baluns with compact physical size while retaining wide fractional bandwidth (FBW) and balanced signal integrity need to be developed [6].

Multilayer printed circuit board (PCB), low-temperature co-fired ceramics (LTCC), monolithic integrated circuits (MMICs), and CMOS, are among the most common integration technologies for the realization of compact planar baluns and many unique design approaches have been demonstrated to date. These include 180° power-dividing baluns using cascaded unit cells [7], [8], [9], power division configurations followed by phase inversion [10], [11], [12], [13], [14], [15], and slot line resonator approaches [16], [17], [18], [19], [20], [21]. Although wide FBWs above 150% have been reported with these techniques, most of the resulting baluns have large physical sizes with footprints ∼0.25 λ_g^2 or larger.

One of the most popular balun types is the Marchand balun (MB). It was first introduced by Nathan Marchand in 1944 using coaxial lines [22] and later converted to a coupled-line implementation, referred to as the compensated MB, by Bawer and Wolfe [23]. This particular topology has achieved BWs up to 15:1 and maximum amplitude imbalance (AI) and phase imbalance (PI) between 0.5 and 1 dB and 5 and 10°, respectively [24], [25], [26], [27]. Like its coaxial line predecessor, it occupies a large footprint of ∼0.25 λ_g^2. Later, a simplified version of these MB concepts, the so-called planar MB was proposed. It consists of only two sections of 0.25 λ_g coupled lines, however, it can achieve FBWs of about 130%, depending on the desired impedance transformation [28]. Various miniaturizations and BW widening techniques have been reported since then achieving FBWs up to 104% and footprints as low as ∼0.003 λ_g^2 [6], [28], [29], [30], [31], [32], [33], [34], [35], [36], [37]. In these architectures, the maximum AI and PI were found to range from 0.2 to 1 dB and 1.8 to 10°, respectively.

To achieve wide FBWs in planar MB configurations, wide coupling coefficients (C) need to be materialized requiring tightly coupled TLs. However, these are difficult to realize in conventional two-layer PCB processes that only facilitate edge-coupled lines with low Cs [32]. With the advancement of thin-layer multilayer PCB and IC processes such as CMOS and MMIC and LTCC, broadside-coupled lines with high Cs are becoming realizable, allowing for wideband responses alongside small physical size due to the high permittivity of their substrates [37]. However, their achievable Cs are limited to finite values only due to the discrete thickness of their layers.

Recently, additive manufacturing (AM) technologies commonly known as 3-D printing are increasingly explored for the manufacturing of RF components. Their design freedom facilitates the realization of practically any shape and 3-D geometry and can be exploited to improve RF performance.

Manuscript received 6 February 2024; revised 27 March 2024; accepted 9 April 2024. This work was supported in part by the Science Foundation Ireland (SFI) under Grant 20/RP/8334 and Grant SFI-13/RC/2077 and in part by Skyworks Inc. *(Corresponding author: Dimitra Psychogiou.)*

The authors are with the Department of Electrical and Electronic Engineering, University College Cork, Cork, T12 K8AF Ireland, and also with Tyndall National Institute, Cork, T12 R5CP Ireland (e-mail: steelejoe99@gmail.com; Dpsychogiou@ucc.ie).

Color versions of one or more figures in this article are available at https://doi.org/10.1109/TMTT.2024.3392434.

Digital Object Identifier 10.1109/TMTT.2024.3392434

Specifically, these processes are not limited by discrete layer thickness, nor do they have the metallization constraints of conventional multilayer processes that rely on particular via shapes to materialize metallic walls. Furthermore, they are not confined to a small number of layers (e.g., 4–8 layers) as is conventionally the case with PCB, MMIC, etc., that constrain the vertical integration of RF components. Thus, a plethora of 3-D printed RF components have been reported to date spanning from antennas [38], [39], [40], [41], [42], [43], reflect-arrays [44], frequency selective surfaces (FSSs) [45], and filters [46]. They are manufactured using various techniques, encompassing continuous liquid interface production (CLIP), [47], stereolithography apparatus (SLA), and selective and laser sintering (SLS) [48]. However, these single-material processes are either suitable for the realization of fully metallic waveguide components or require post-processing for the metallization of their plastic parts using sputtering or electroplating. These techniques, therefore, are typically only suitable for the realization of fully metallic components.

For RF components requiring both conductive and dielectric materials, inkjet-based AM is more suitable and is increasingly being explored as a manufacturing alternative. This AM technique has been used extensively in the realization of patch antennas [49], [50], [51], [52], [53], [54], [55]. However, most of these processes are limited to one or two materials and can only produce a single or few vertically stacked layers, resulting in very thin substrates (1–3.5 μm thick) that cannot easily be used for the realization of 3-D RF components that require mm-scale thicknesses. A very promising multilayer inkjet-based process using silver-based ink and dielectric ink was recently developed [56]. It facilitates thin and thick substrates to be realized by combining multiple dielectric and metallic layers and can be exploited for the realization of vertically integrated components. Alternative component demonstrations have been shown using this manufacturing technology including antennas [57], [58], metasurfaces [59], [60], [61], interdigital capacitors [71], and bandpass filters to frequencies as high as 20 GHz.

Taking into consideration the enabling capabilities of inkjet printing, and the design limitations in MBs, this manuscript investigates for the first time, the potential to realize wideband and highly miniaturized MBs using inkjet printing and tightly coupled broadside-coupled lines. Additionally, the manuscript presents a comprehensive design methodology and an optimization method determining the maximum achievable FBW. Several TL-based integration concepts are analyzed using 2-D and 3-D EM simulations to specify the required impedances and Cs that maximize FBW while taking into consideration the process capabilities of a multimaterial multilayer inkjet printing process which is used in this work for the realization of MBs for first time. A miniaturization scheme using spiral TLs and slanted vias is also explored for size compactness. To validate this approach, several coupled-line test structures and MBs were designed, manufactured, and tested.

The manuscript is organized as follows. Section II presents a comprehensive design methodology for maximum FBW realization alongside practical realization effects. In Section III, the practical validation of the concept through a number of test structures and MB realizations is presented. Lastly, Section IV summarizes the major contributions of this work.

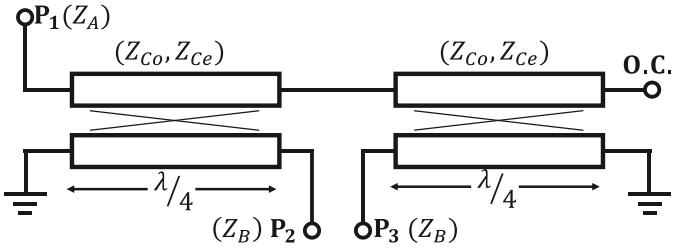

Fig. 1. Circuit schematic of a planar MB. P_1: Unbalanced port with characteristic impedance Z_A. P_2 and P_3: Balanced ports with characteristic impedance Z_B. All coupled lines are 90° long at f_0 and have a characteristic impedance Z_C and coupling coefficient C.

II. Theoretical Foundations

A. BW Limits of MBs

The circuit schematic details of an MB are provided in Fig. 1. It consists of two quarter-wavelength ($\lambda_g/4$) coupled lines (specified at the center frequency f_0) that transform an unbalanced RF signal (applied to Port 1) to a balanced one (between Ports 2 and 3) alongside providing an impedance transformation between Z_A (the impedance of Port 1) and Z_B (the impedance of Ports 2, 3). MBs are designed to satisfy $S_{21} = -S_{31}$ while being perfectly matched at their input, i.e., $S_{11} = 0$ at f_0. All conditions can be met when the even and odd-mode impedances of the $\lambda/4$ coupled lines (Z_{Co}, Z_{Ce}) satisfy (1) [28]

$$\frac{1}{Z_{Co}} - \frac{1}{Z_{Ce}} = \sqrt{\frac{1}{Z_A Z_B}}. \tag{1}$$

Using the equivalences for the coupling coefficient (C) and the characteristic impedance (Z_C) of the coupled lines in the first equation that follows, an expression can be derived for the optimal Z_C in the second equation that follows:

$$C = \frac{Z_{Ce} - Z_{Co}}{Z_{Ce} + Z_{Co}}, \quad Z_C = \sqrt{Z_{Ce} Z_{Co}} \tag{2}$$

$$Z_C(C) = \sqrt{2 Z_A Z_B} \frac{C}{\sqrt{1 - C^2}}. \tag{3}$$

whereas these expressions allow calculating C, Z_C for a perfect impedance matching at f_0,they do not provide any insight on the operational FBW of the MB, that is, the range of frequencies where $|S_{11}|<-10$ dB while having perfect amplitude balance $|S_{21}| = |S_{31}|$ and phase balance of 180° (or an acceptable threshold for practical applications). Thus, the FBW needs to be calculated by computing its S-parameters using ideal linear circuit simulations (e.g., in Keysight's Advanced Design System (ADS) [64]).

To get a better picture of the FBW performance capabilities of the MB, a parametric study over C, Z_B in steps of 0.01 and 2.5 Ω, respectively, was performed and is provided in Fig. 2(a). As shown, FBWs > 100% can be clearly obtained for $C > 0.6$, while the maximum possible FBWs of about 135% occur around $C \approx 0.7$ for $Z_B > 100$ Ω. To illustrate the possible FBW trends further, three specific cases are

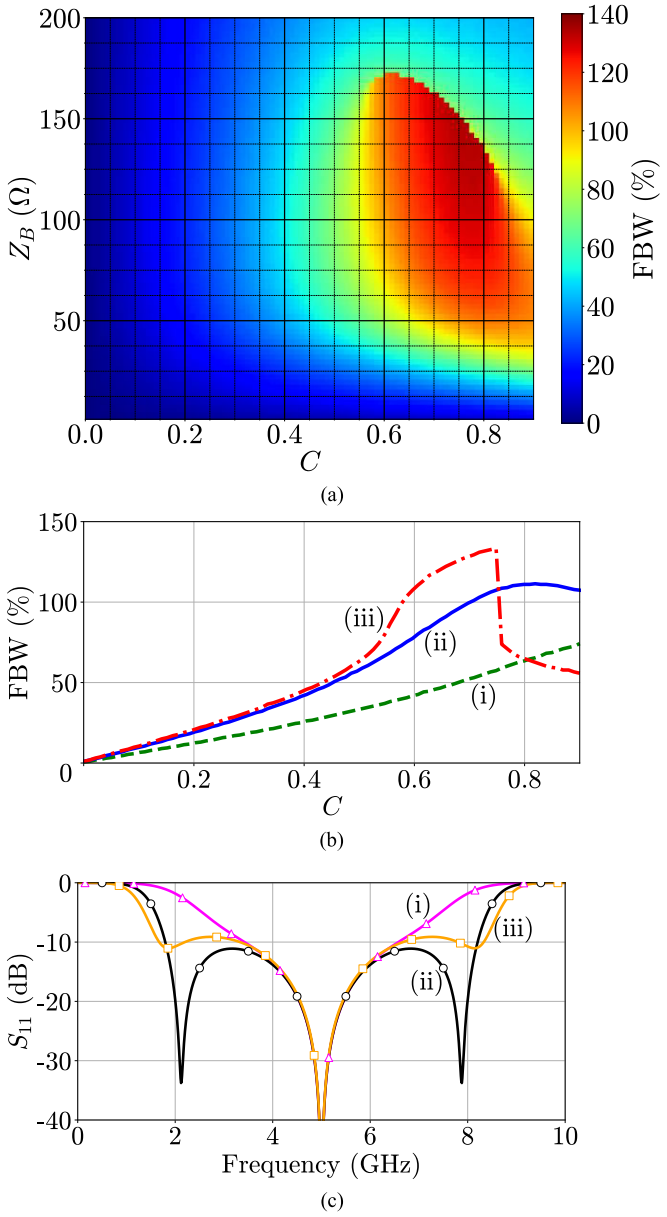

Fig. 2. FBW and reflection coefficient ($|S_{11}|$) of the MB topology in Fig. 1 as a function of Z_B. (a) Heatmap of FBW over the (C, Z_B) parameter space. (b) FBW as a function of C for three Z_B example cases. Case (i) Z_B = 25 Ω, case (ii) Z_B = 50 Ω, and case (iii) Z_B = 150 Ω. (c) Three example frequency responses of $|S_{11}|$ for Z_B = 150 Ω and varying C. Case (i) C = 0.5, case (ii) C = 0.7, and case (iii) C = 0.8.

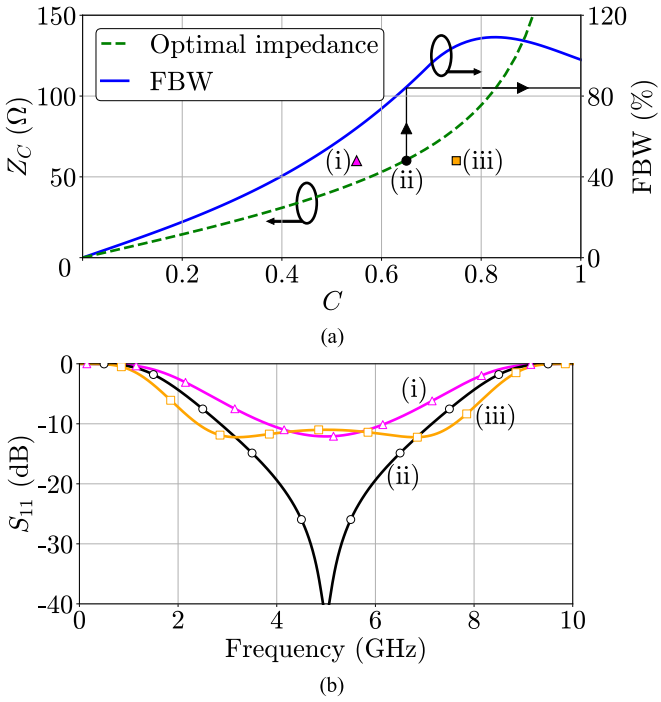

Fig. 3. (a) Optimal required Z_C (dashed green line) of the MB in Fig. 1 as a function of C using (3) and its resultant FBW calculated from (4). (b) Corresponding frequency response $|S_{11}|$ for three (C, Z_C) example cases with a fixed Z_C = 60 Ω. Case (i): C = 0.55, case (ii): C = 0.65,(ideal), and case (iii), C = 0.75. In all these examples Z_A = Z_B = 50 Ω.

provided in Fig. 2(b). As shown, for lower impedances such as Z_B = 25 Ω in case (i), only FBWs below 62% are possible, whereas for the most common case in the literature, i.e., Z_B = 50 Ω in case (ii), the FBW increases with C and reaches an ultimate maximum of 109% for C = 0.83 and Z_C = 105 Ω. However, such high Cs cannot be realized even in advanced commercially available processes such as PCB, LTCC, MMIC, CMOS, etc., (typically below 0.75 [32], [65]), thus the actual FBW in practice is narrower. Case (iii) presents the FBW trends for Z_B = 150 Ω, where a sharp decrease in the FBW is observed shortly after its maximum for C = 0.75 in Fig. 2(b). This sharp drop can be better explained by examining the S-parameter performance in Fig. 2(c) for Z_B = 150 Ω and by varying C. As can be seen, the FBW increase starts to get limited when the reflection zeros at the edges move further away from the center frequency and result in finite reflection. This can also be observed in practice in the MB configuration in [34] that has been implemented for Z_B = 150 Ω (see Fig. 3).

As Z_A = Z_B = 50 Ω is the most common MB implementation [28], [29], [30], [31], [32], [36], [37], [66], [67], [68], [69], [70], this manuscript will focus on its realization using inkjet printing and will aim to maximize its FBW. Its corresponding performance is illustrated in detail in Fig. 3. Based on the obtained relationship between FBW and C in Fig. 3(a), it can be approximated using the piecewise function in the following equation that was obtained by interpolating ten extracted pairs of C, FBW:

$$\mathrm{FBW}(C) = \begin{cases} 118C^3 - 8.25C^2 + 85.5C, C \le 0.7 \\ 1371C^3 - 4018C^2 + 3834C - 1089, C > 0.7. \end{cases} \quad (4)$$

It can be observed that as C increases, FBW also increases, reaching its maximum of 109% when C = 0.83, and decreasing thereafter. Thus, it is not generally the case that maximizing C will result in a maximum FBW, as is typically the rule of thumb of the open technical literature. It should be further emphasized that (4) describes the FBW for perfect matching at f_0, for a given C and corresponding Z_C prescribed by (3). If coupled lines with C, Z_C not satisfying (3) are used, then the matching at f_0 is compromised and may lead to narrower or wider FBWs as shown in Fig. 3(b) for three design cases. The significantly degraded matching at f_0 = 5 GHz in cases (i) and (iii) compared to perfect matching in case (ii)

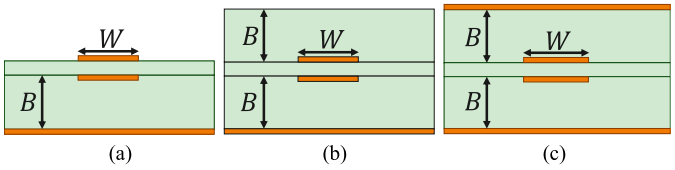

Fig. 4. Broadside-coupled line types. (a) MS, (b) EMS, and (c) SL.

demonstrates the necessity of accurately calculating coupled-line parameters for the process that is being used.

B. Broadside-Coupled Lines Design Process

To achieve high couplings alongside a small footprint in practice, broadside-coupled TLs are typically preferred to their edge-coupled counterparts due to their Cs being significantly higher. Three different geometries, namely microstrip [MS, in Fig. 4(a)], embedded microstrip [EMS, in Fig. 4(b)], and stripline [SL, in Fig. 4(c)] are considered and are shown in Fig. 4. Their performance is determined by considering the capabilities of the inkjet process in [56] with the minimum spacing (S) being the most critical factor. Specifically, the process allows for two different materials to be printed in the same manufacturing platform, namely an acylate-based dielectric ink with relative permittivity (ε_r) ~2.83 and dielectric loss tangent tan(δ) ~ 0.023 at 5 GHz, and a silver nanoparticle conductive ink with conductivity σ between 1.8×10^6 and 2.52×10^7S/m [56], [62], [71]. All initial simulations were performed using the nominal value in the data sheet as 2.21×10^7S/m [56]. Furthermore, the process allows for trace widths > 75 μm and trace-to-trace spacings > 100 μm. Small dielectric layer thicknesses are also possible with the minimum achievable dielectric thickness being dependent on the thickness of the metallization layer. In this case, a metallization thickness of 17 μm (3–11$\times$ the skin depth at 5 GHz) is used, allowing the minimum dielectric thickness to be equal to 50 μm.

Considering the aforementioned process capabilities, various TL geometries were analyzed using 2-D and 3-D EM simulations in ANSYS in order to extract their Z_C and C values as a function of various geometrical parameters, i.e., the width of the traces (W) and the distance between the traces and the ground (B). These are summarized in Figs. 5 and 6 for $S = 50$ μm (the minimum layer thickness). A wide range of Z_C and C can be obtained by freely altering B, an advantage to be highlighted as opposed to conventional PCB, LTCC, and MMIC processes that have finite and discrete layer thicknesses, preventing a continuous range of Z_Cs and Cs to be obtained.

The 2-D EM in Fig. 4 simulations were performed on the same coupled-line structures using the Q3D 2-D extractor from ANSYS that allows to extract the R, L, C, and G parameters of the TL [72]. They can be used to calculate the odd- and even-mode capacitances and inductances of the TL using the following equation where labels 1 and 2 denote the upper and the lower conductor, respectively:

$$\begin{aligned} C_o &= 0.5(C_{11} + C_{22} - C_{12} - C_{21}) \\ C_e &= 0.5(C_{11} + C_{22} + C_{12} + C_{21}) \\ L_o &= 0.5(L_{11} + L_{22} - L_{12} - L_{21}) \\ L_e &= 0.5(L_{11} + L_{22} + L_{12} + L_{21}) \end{aligned}. \quad (5)$$

TABLE I
COUPLED-LINE PARAMETER RANGES PLOTTED IN FIG. 6

Case	C	Z_C (Ω)	FBW (%)
(a) MS	0.61-0.78	54-88	76-107
(b) EMS	0.59-0.76	52-83	72-105
(c) SL	0.50-0.71	41-71	55-99

Subsequently, the odd- and even-mode characteristic impedances (Z_{Co}, Z_{Ce}) can be specified using the following equation:

$$Z_{Co} = \sqrt{\frac{L_o}{C_o}}, \quad Z_{Ce} = \sqrt{\frac{L_e}{C_e}}. \quad (6)$$

Z_C and C can also be calculated using 3-D EM simulations in ANSYS HFSS by exciting the $\lambda/4$ coupled lines with differential ports at each end. This allows for the accurate calculation of the common mode impedance (Z_{Comm}) and the differential mode impedance (Z_{Diff}). Then Z_{Co} and Z_{Ce} can be computed using the following equation and Z_C and C using (2):

$$Z_{Co} = 0.5Z_{\text{Diff}}, Z_{Ce} = 2Z_{\text{Comm}}. \quad (7)$$

A comparison between the two methods is provided in Fig. 5 for all three different TLs which are in good agreement. It should be noted that the 2-D method requires less computational time and is typically quicker to set up, while 3-D simulations were found to be more accurate for balun synthesis. Having determined the Z_C and C characteristics of each TL, their optimal values for maximizing the FBW of the MB can be specified graphically. After overlaying the FBW(C) and the $Z_C(C)$ relationships in (3) and (4) on the same plot, the region of intersection with the computed values of (C, Z_C) and (3) is found as shown in Fig. 6. The design parameter ranges for MS, EMS, and SL TLs are provided in Table I. As expected, the largest Z_C and C are obtained for the MS coupled lines, leading to an optimal FBW of 107%. The lowest Z_C and C were obtained for the SL coupled lines leading to a nearly optimal maximum FBW of 99%. As noticed, the EMS performance is in between these two. Although the MS coupled lines are expected to give a slightly higher FBW, they have higher dispersion and may lead to higher AI and PI when used to materialize an MB [73] and may narrow its actual FBW. Thus, SL is used for the practical realization of the inkjet-printed MBs with $C = 0.71$, $Z_C = 71$ Ω, indicated by the red marker in Fig. 6(c). This corresponds to a $W = 115$ μm, $B = 500$ μm, and is expected to lead to an FBW = 99%.

C. Practical Realization Aspects

To practically realize the MB, an interconnecting line (Z_{conn}, θ_{conn}) as shown in Fig. 7, needs to be added between the two upper sections to facilitate the realization of the P_2, P_3 outputs that would otherwise fall on top of each other. Additionally, this line can help to balance the AI and PI that is caused due to the dispersion of the coupled lines as discussed in [6]. For perfectly homogenous coupled lines with identical

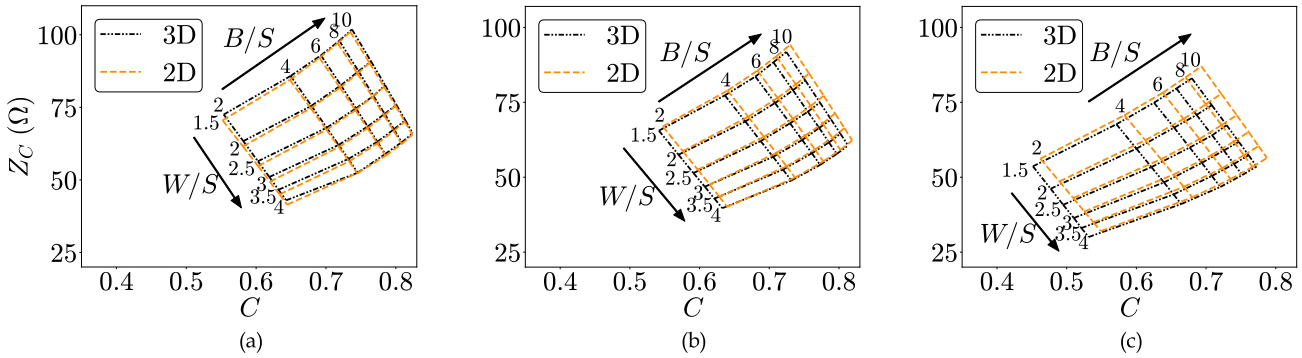

Fig. 5. Z_C and C for three types of broadside-coupled lines as a function of the ratios W/S and B/S using the 2-D RLCG extraction method and full 3-D EM simulations. (a) MS geometry shown in Fig. 4(a). (b) EMS geometry shown in Fig. 4(b). (c) SL geometry shown in Fig. 4(c).

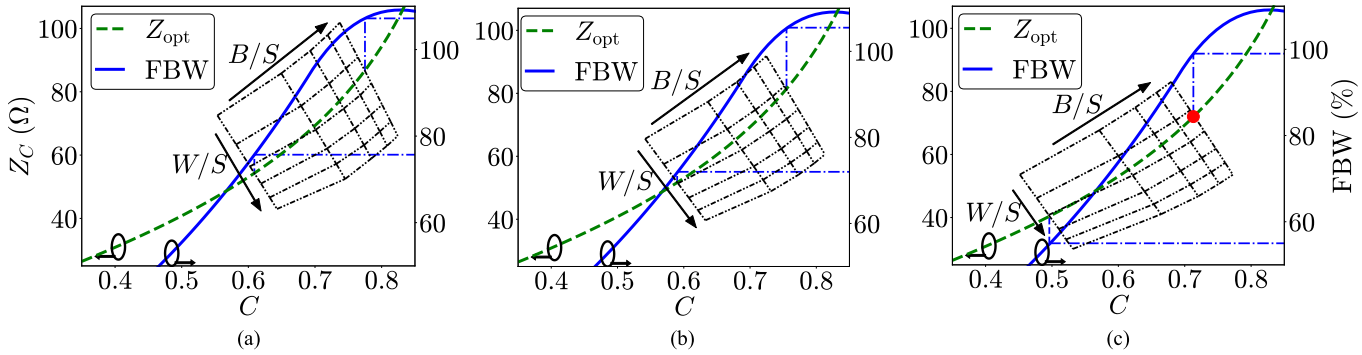

Fig. 6. Z_C and C for three types of broadside-coupled lines as a function of the ratios W/S and B/S calculated using full 3-D EM simulations. They are overlaid on the optimal Z_C and FBW curves given by (3) and (4). (a) MS geometry shown in Fig. 4(a). (b) EMS geometry shown in Fig. 4(b). (c) SL geometry shown in Fig. 4(c).

odd- and even-mode phases θ_o, θ_e, perfect AI and PI can be obtained for $\theta_{\text{conn}} = 0$. However, this is never the case in practice due to the uneven phase velocities. It is then useful to design the connecting line to counteract the uneven θ_o, θ_e and improve the balun's AI and PI using (8) [6], which gives a design curve of possible $(\theta_{\text{conn}}, Z_{\text{conn}})$ pairs which ensure $S_{21} = -S_{31}$ at f_0

$$\frac{1}{Z_{\text{conn}}}\tan\left(\frac{\theta_{\text{conn}}}{2}\right) = \frac{\cot(\theta_e)\csc(\theta_o) - \cot(\theta_o)\csc(\theta_e)}{Z_{Ce}\csc(\theta_o) - Z_{Co}\csc(\theta_e)}. \quad (8)$$

This method however requires the calculation of θ_o, θ_e which can be difficult to calculate using equation-based approaches, especially if using a more complex coupled-line structure. Thus, the full 3-D EM extraction approach in Section II-B is used to obtain θ_o, θ_e. Specifically, θ_o, θ_e are respectively the common mode phase (θ_{Comm}) and the differential mode phase (θ_{Diff}) of these coupled lines at f_0 which can be calculated using the following equation:

$$\theta_{\text{Comm}} = \angle S_{cc21}, \quad \theta_{\text{Diff}} = \angle S_{dd21} \quad (9)$$

where S_{cc21} and S_{dd21} are the common and differential mode power transmission coefficients [79]. The chosen SL parameters were calculated as $\theta_o = 88.6°, \theta_e = 91.9°$. If the connecting length is known, for example, $L_{\text{conn}} = 500$ μm, first $\theta_{\text{conn}} = 4.5°$ is calculated, leading to a $Z_{\text{conn}} = 65$ Ω, which corresponds to a width $W_{\text{conn}} = 130$ μm.

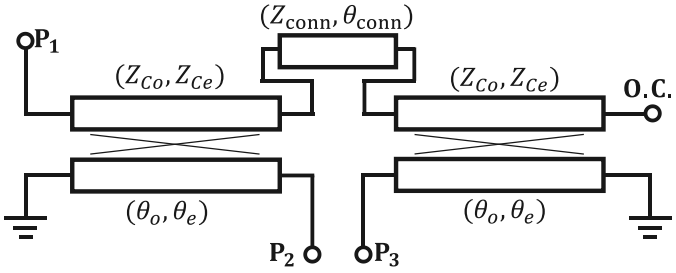

Fig. 7. Adapted circuit schematic of the MB in Fig. 1, including the necessary connecting line for a practical implementation having characteristic impedance Z_{conn} and electrical length θ_{conn}.

D. MBs Using Straight Coupled Lines

Using the process design guidelines as a reference and full-wave EM simulations in ANSYS HFSS, an MB was designed and is shown in Fig. 8(a) and (b). The addition of the interconnecting line leads to a perfect matching at the center frequency and a small FBW deterioration from 99% to 97%, which is the targeted maximum FBW for the experimental prototype. Straight coupled-line sections are used in this case and are folded side-by-side for size compactness, leading to an overall footprint of $L_{\text{St}} \times W_{\text{St}} \times H = 8.2 \times 1.35 \times 1.12$ mm^3. The RF signal is connected to the coupled lines through a vertical transition that is realized with a 3-D via whose size and shape are optimized for minimum reflection loss. The 3-D vertical transition is optimized by analyzing its

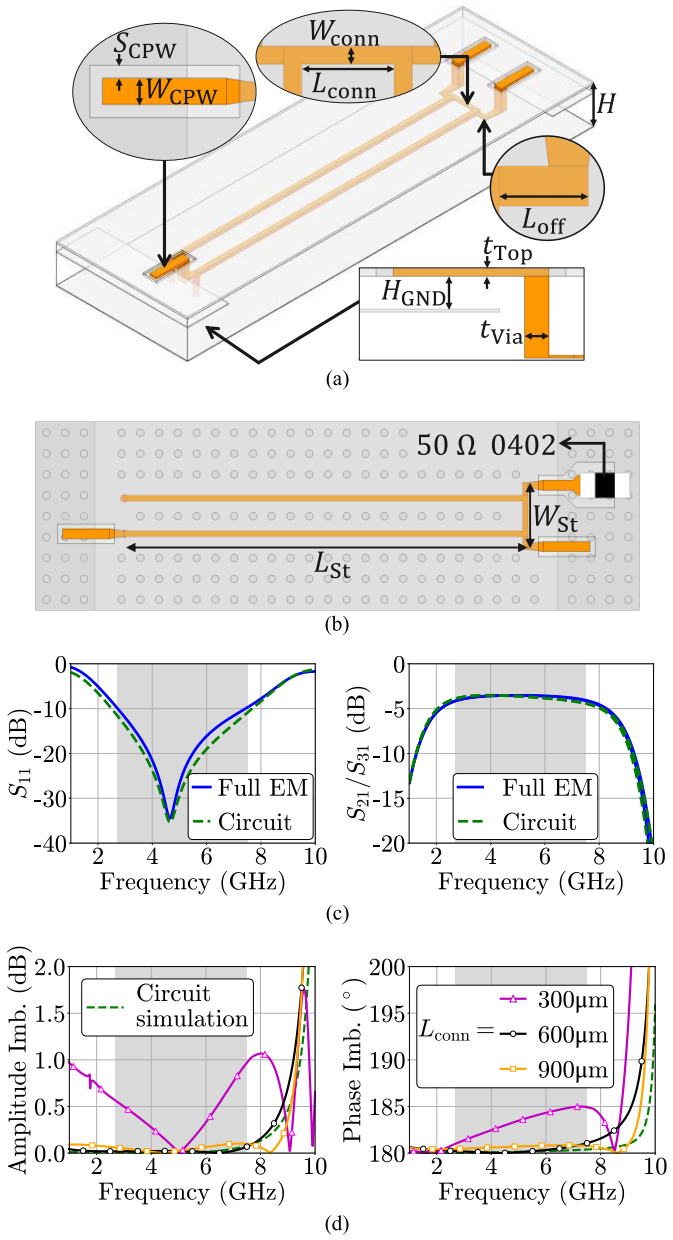

Fig. 8. (a) Bird's eye view of the 3-D geometry and EM simulation model for the inkjet-printed MB based on broadside-coupled straight SLs where L_{conn} = 500 μm, W_{conn} = 130 μm, W_{CPW} = 200 μm, S_{CPW} = 100 μm, H_{GND} = 187 μm, L_{off} = 260 μm, t_{Top} = 50 μm, t_{Via} = 150 μm, and $H = 2B + S + t + t_{Top}$ = 1117 μm. Orange layers: broadside SL coupled lines materialized with conductive ink. Light gray layers: ground planes materialized with conductive ink. Transparent layers: dielectric ink. (b) Top-view of inkjet-printed MB based on broadside-coupled straight SLs where L_{St} = 8.2 mm and W_{St} = 0.83 mm. (c) Ideal circuit simulation including the connecting line with θ_{conn} = 4.5°, Z_{conn} = 65 Ω and EM-simulated transmission with L_{conn} = 600 μm and W_{conn} = 130 μm. (d) Full EM-simulated AI and PI of the straight balun given in (a) for fixed W_{conn} = 130 μm and varying L_{conn}.

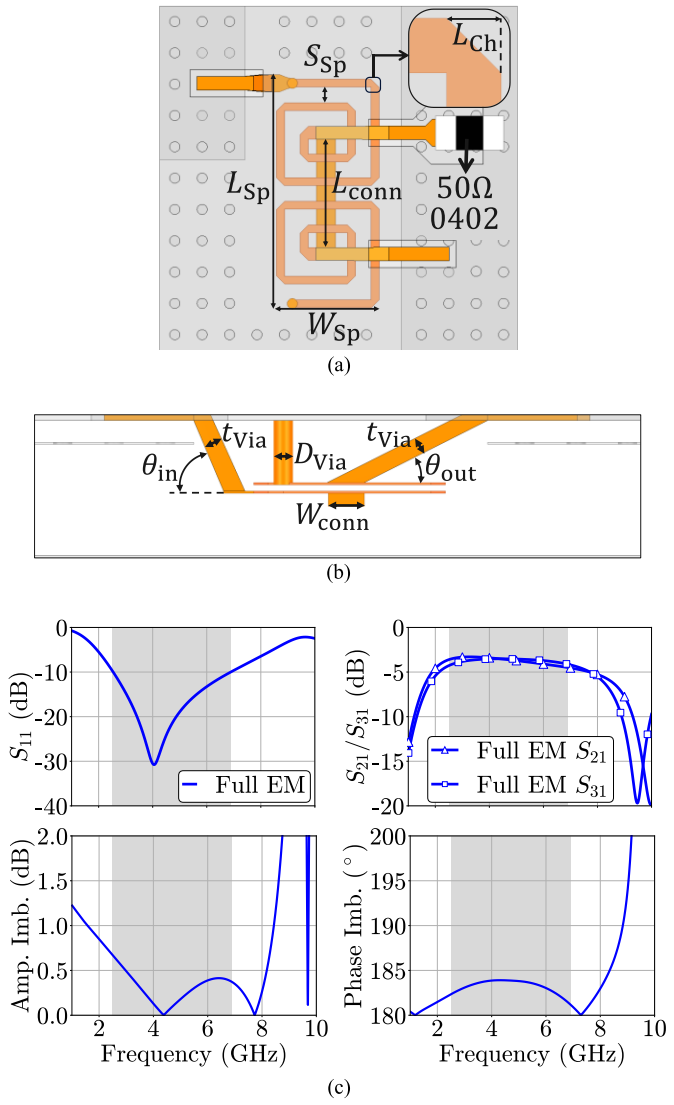

Fig. 9. (a) Top view of the 3-D geometry and EM simulation model for the inkjet-printed MB based on broadside-coupled spiraled SLs where L_{conn} = 1600 μm, L_{Ch} = 115 μm, S_{Sp} = 230 μm, L_{Sp} = 3350 μm, and W_{Sp} = 1530 μm. (b) Side view of geometry where t_{Via} = 150 μm, W_{conn} = 260 μm, D_{Via} = 150 μm, θ_{in} = 67°, and θ_{out} = 27°. (c) Comparison between EM-simulated, and ideal circuit-simulated S_{11} responses and full EM-simulated S_{21}/S_{31}, AI, and PI for C = 0.71, Z_C = 71 Ω, θ_{conn} = 15° and Z_{conn} = 50 Ω, or L_{conn} = 600 μm and W_{conn} = 130 μm.

reflection coefficient. It was found that having the widths of the 3-D vertical transition equal to the terminating CPW width (W_{CPW} = 200 μm) minimized reflection losses. A tapered transition from the coupled-linewidth (W = 115 μm) to the 3-D via was used to further minimize reflections.

Grounding vias are also used to interconnect the bottom ground with the ground plane of the grounded coplanar waveguide (GCPW) of the RF input/output ports as shown in Fig. 8(b). They have been omitted in Fig. 8(a) for clarity. The placement of the ground plane of the GCPW ports takes advantage of the design freedom along the z-axis to facilitate excitation using 250 μm GSG probes. Specifically, using the minimum trace-to-trace spacing S_{CPW} = 100 μm, a trace width of W_{CPW} = 200 μm allows for 250 μm GSG probes to properly contact the trace and the ground plane. The impedance of the GCPW can be controlled by H_{GND}. Thus, the required value for H_{GND} can be extracted parametrically and a value of 187 μm was chosen for a 50 Ω GCPW impedance.

Fig. 8(c) demonstrates the EM-simulated S-parameters of the MB alongside the ones obtained by linear circuit simulations for the same parameters (C = 0.71, Z_C = 71 Ω, θ_{conn} = 4.5°, and Z_{conn} = 65 Ω respectively). As shown, they are in good agreement successfully validating the proposed design

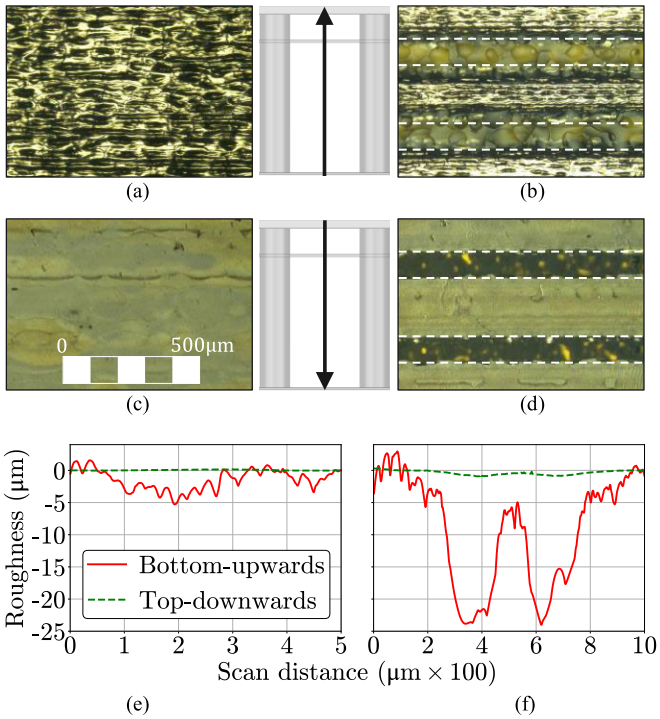

Fig. 10. Optical images and surface roughness measurements of the manufactured MBs for two different printing orientations, i.e., bottom-upward [in (a) and (b)] and top-downward [in (c) and (d)]. The images zoomed-in view into a small metal area [in (a) and (c)] and around a GCPW on the top of the test coupon [in (b) and (d)]. The ideally designed CPWG profile lines for $W_{\text{CPW}} = 200$ μm and $S_{\text{CPW}} = 100$ μm,are overlaid as dashed white lines. (a) and (b) Magnified detail of the metal and the GCPW area of a test coupon printed bottom-upward and cross section of the coupon showing the printing orientation. (c) and (d) Magnified detail of a test coupon printed top-downward and cross section of the coupon showing the printing orientation. (e) Surface roughness in of the metal area. (f) Surface roughness of the GCPW area.

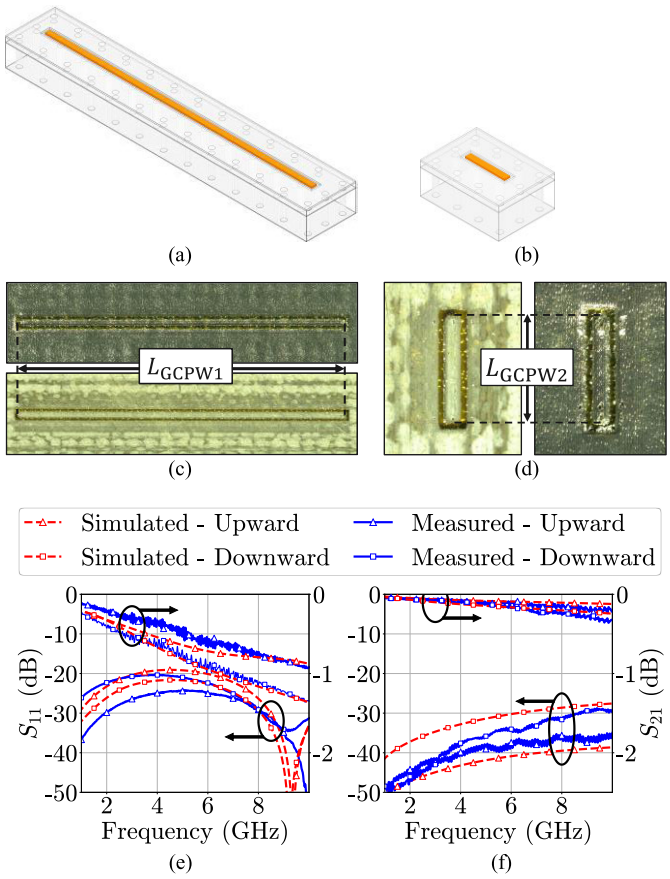

Fig. 11. Characterization of GCPW TLs having two different lengths. (a), (c), and (e) Layout, photograph, and EM-simulated and RF-measured S-parameters of the longer GCPW with $L_{\text{GCPW1}} = 10\,750$ μm for two different printing directions: bottom-upward (upper image) and top-downward (lower image). (b), (d), and (f) Layout, photograph, and EM-simulated and RF-measured S-parameters of the GCPW with $L_{\text{GCPW2}} = 1400$ μm printed bottom-upward (right image) and top-downward (left image), and RF-measured S-parameters for each print direction.

methodology. Minor differences are observed in the obtained FBW which was calculated around 97% in the circuit simulations as opposed to 95% in EM simulations. These are to be expected considering the added parasitics from the required junctions and bends in the realistic prototype. Furthermore, Fig. 8(d) demonstrates the effect of the connecting line on the AI an PI in full EM simulations when varying away from its optimal value $L_{\text{conn}} = 600$ μm. In summary, the EM-simulated MB exhibits the following RF performance characteristics: FBW = 95%, AI < 0.13 dB, and PI $< 1.3°$ throughout this BW.

E. Miniaturized MB Using Spiral Lines

Taking into consideration the free-form manufacturing capabilities of the two-material multilayer inkjet printing process, 3-D vertical integration alongside spiraling can be considered for size compactness. Fig. 9(a) and (b) depicts the 3-D geometry of the resulting MB that has a footprint of $0.043 \times 0.094 \times 0.028$ λ_g^3 that is two times smaller than the MB based on straight coupled lines in Fig. 8. Considering that spiraling of the coupled lines can affect the MB's AI and PI due to altering their odd- and even-mode phase velocities [74], prior to starting the design of the MB, the characteristic parameters of the interconnecting line need to be recalculated using the design method in Section II-C and 3-D EM simulations. It should be emphasized that in this case, the exact spiraled TL configuration that is used in the MB must be simulated so that correct phases are obtained and for a $L_{\text{conn}} = 1600$ μm to allow for a proper layout of the MB. These values are as follows: $\theta_o = 84.6°$, $\theta_e = 97.9°$, and $W_{\text{conn}} = 260$ μm leading to an overall footprint of $L_{\text{Sp}} \times W_{\text{Sp}} \times H = 3.35 \times 1.53 \times 1.12$ mm^3.

The EM-simulated performance of the spiraled-line MB is provided in Fig. 9(c) and is summarized as follows: FBW = 95%, where AI $= 0.35 \pm 0.35$ dB, and PI $= 2 \pm 2°$ over this FBW. As shown, the connecting line has allowed for good AI and PI to be obtained in the passband, but there is clear degradation compared to the straight coupled-line case. This is expected due to the induced parasitics, and current crowding introduced by spiraling the coupled lines.

III. Experimental Validation

To validate the potential of the two-material inkjet printing process for the proposed MB designs, various test structures and balun prototypes were manufactured and tested using Agilent E5071C VNA and 250 μm GSG probes. These include two GCPW TLs, two GCPW-to-SL transitions with vertical

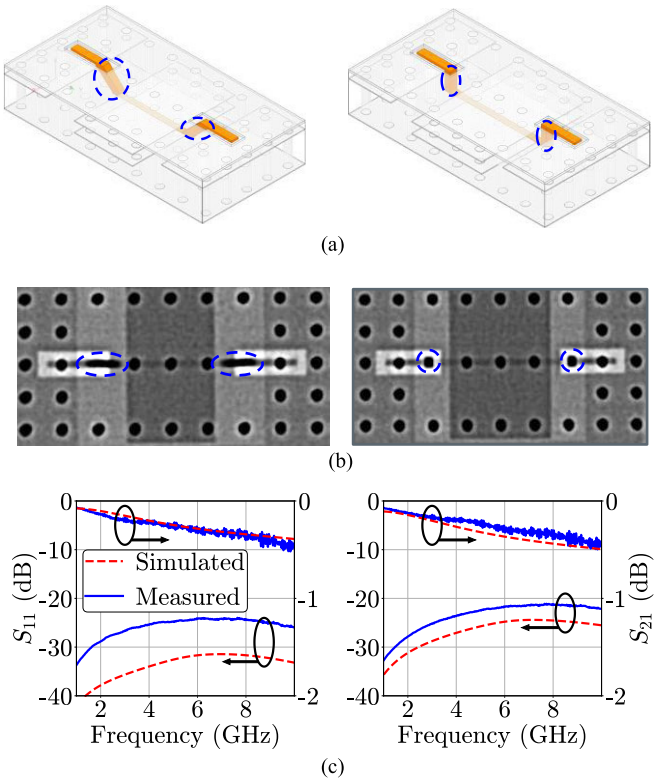

Fig. 12. Characterization of 3-D vertical and sloped via transition test structures. (a) Three-dimensional EM models of the slanted transition (left) and the vertical transition (right) with transitions indicated with dashed circles. (b) Top view of X-ray scans of the slanted transition (left) and the vertical transition (right). (c) EM-simulated and RF-measured S-parameters of the slanted transition (left) and the vertical transition (right).

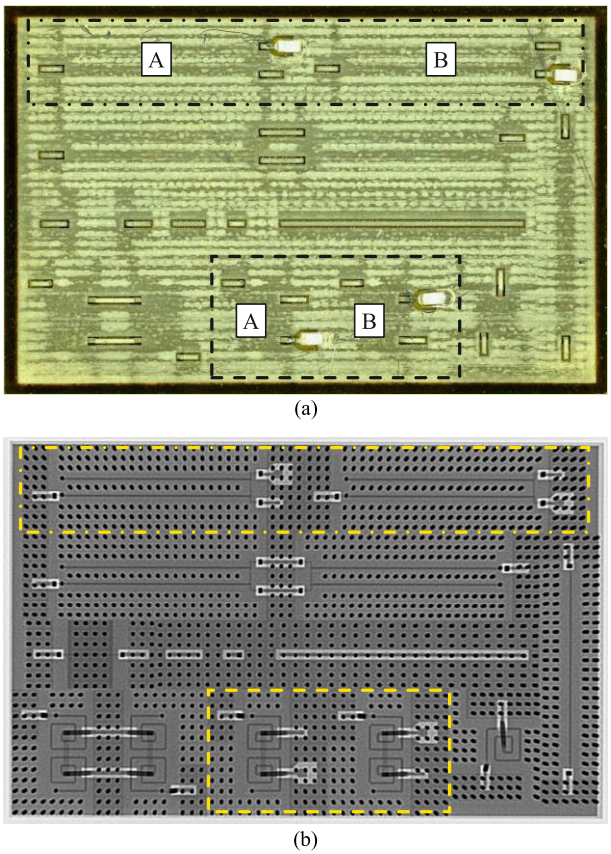

Fig. 13. Optical scans of test coupons that include multiple devices and test structures. Example devices of the straight coupled-line (dot-dash lines) and the spiraled-coupled line (dashed lines) baluns are indicated on each board. (a) Top view of an optical scan where resistive terminations using 0402 resistors have been soldered on. (b) X-ray view displaying internal structures underneath the top ground plane.

and slanted 3-D vias, an MB using straight broadside-coupled TLs, and a miniaturized MB using spiraled broadside-coupled TLs. Furthermore, the spiral balun was tested in a back-to-back configuration.

A. Test Structures

The 3-D geometries, RF-measured and EM-simulated S-parameters, and the surface profile of the test structures are provided in Figs. 10–12. Specifically, Fig. 10 illustrates the surface profile details of example test areas on the manufacturing coupons. Fig. 11 displays the 3-D geometry, the manufactured prototype, and the RF-measured and EM-simulated performance of two GCPW TLs having two different lengths of $L_{\text{GCPW1}} = 10.75$ mm [see Fig. 11(a), (c), (e)] and $L_{\text{GCPW2}} = 1.4$ mm [see Fig. 11(b), (d), (f)] when printed bottom-upward and top-downward as shown in Fig. 10. It can be observed that the test structures printed top-downward exhibit less loss. This is due to the top layers of the GCPW being the first layers that are printed, thereby being directly attached onto the build plate which allows for a smooth surface to be obtained. To verify this further, Fig. 10 provides magnified optical images and the measured surface roughness of sample areas around the test samples for a fully metalized area away from the GCPW and around the GCPW for the two different print orientations. They were obtained using a Tencor P10 surface profiler. In the bottom-upward orientation in Fig. 10(a), the roughness average of the surface (R_a) varies between 1.8 and 4.2 μm whereas in the top-downward orientation in Fig. 10(b), it varies between 0.04 and 0.2 μm. Taking several sample profiles over various regions on each coupon, an average $R_a \approx 2$ μm was estimated for the bottom-upward prototypes and $R_a \approx 0.1$ μm for the top-downward ones. In addition to the roughness, the printing orientation also affects the dimensions of the GCPW as evidenced in Fig. 10(b) and (d). As noticed in the bottom-upward case, the GCPW profile deviates from the desired dimensions (marked with white dashed lines for clarity) with the gaps between the inner and the outer grounds being wider than expected, possibly leading to additional reflection loss as shown in Fig. 11(e) and (f). The GCPW profile quality is provided in Fig. 10(f). As shown in the bottom-upward orientation, significant differences of up to 25 μm can be observed from the expected perfectly flat surface. Fig. 11(e) and (f) also include the EM-simulated responses of the test structures for alternative levels of roughness. A good agreement is obtained between the EM-simulated and the RF-measured responses when using the measured R_a values of 0.1 μm for the top-downward case and $R_a = 2$ μm for the bottom-upward case in combination with a conductivity $\sigma = 1.8 \times 10^6$ Sm^{-1} [71]. Taking into consideration that the printing orientation affects

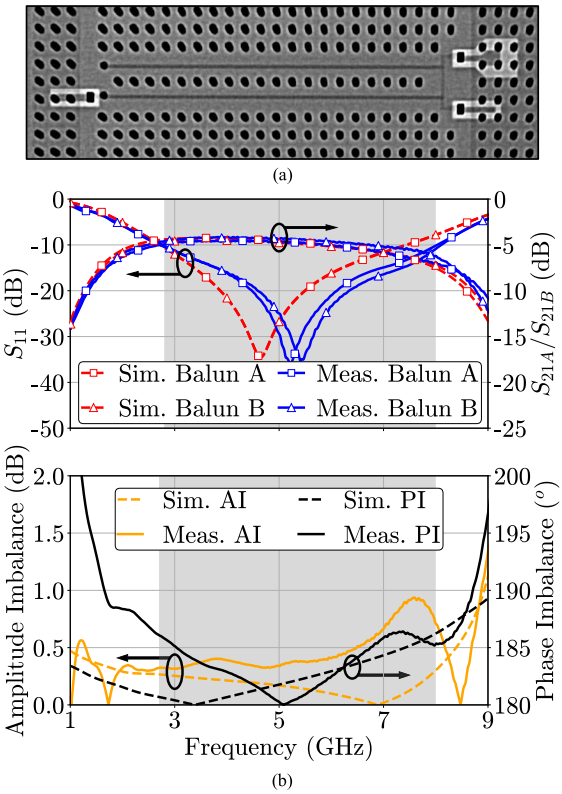

Fig. 14. Resistively-terminated SL-based straight MB alongside its corresponding EM-simulated and RF-measured S-parameters, AI, and PI. (a) X-ray image of the manufactured SL-based straight MB (Balun A) with P_3 terminated to a 50 Ω 0402 resistor. The MB with resistive termination at port 3 (Balun B) has been omitted due to their similarity. The circles indicate the grounding vias. (b) EM-simulated and RF-measured S-parameters (top) of two resistively-terminated MBs (Balun A: Corresponding to S_{21A} where P_3 is resistively-terminated, Balun B: Corresponding to S_{21B} where P_2 is resistively-terminated) and calculated EM-simulated and RF-measured AI and PI. The shaded gray area indicates the operational BW.

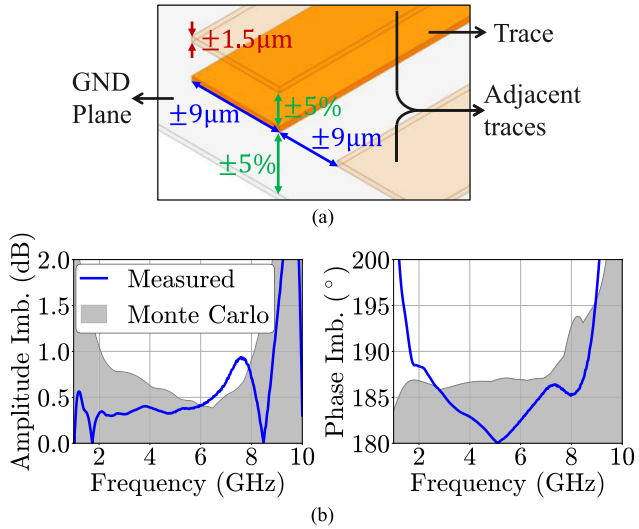

Fig. 15. (a) Illustration of potential tolerance variations. (b) Resulting AI and PI between Balun A and Balun B estimated by Monte Carlo simulations with the RF-measured AI and PI overlayed. In these examples, $R_a = 2$ μm and $\sigma = 1.8 \times 10^6$ S/m are considered.

RF performance, the top-downward approach was used for the manufacturing of the rest of the test structures and devices.

To investigate the quality of the vertical transitions, two test structures, namely: i) a GCPW-to-SL transition using a vertical 3-D via and ii) a GCPW-to-SL transition with a slanted 3-D via were manufactured and tested in a back-to-back configuration using a 17° (at 5 GHz) long piece of SL and are shown in Fig. 12(a). X-rays of their prototypes are shown in Fig. 12(b) with the transitions being indicated with dashed lines. Their EM-simulated and RF-measured S-parameters are provided in Fig. 12(c) and appear to be in good agreement, successfully validating the manufacturing process that leads to broadband (1–10 GHz), well-matched, and low-loss transitions. The agreement gives further evidence as to the validity of the material parameters used in the simulation and using these simulations as a reference, the loss of the slanted and vertical structures was estimated at 0.11 and 0.12 dB at 5 GHz, respectively.

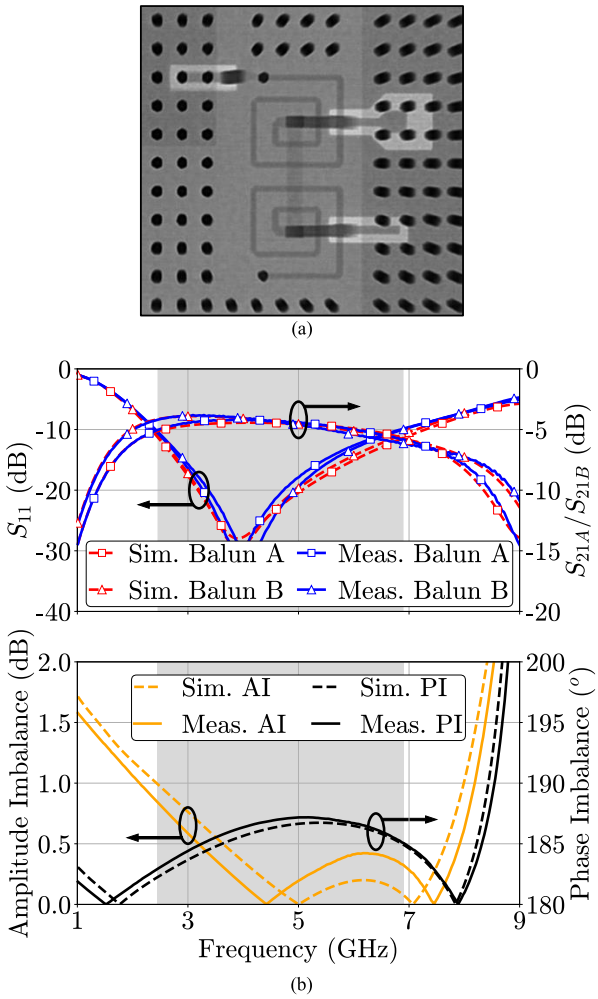

Fig. 16. Resistively terminated spiral MB alongside its corresponding EM-simulated and RF-measured S-parameters, AI, and PI. (a) X-ray image of the manufactured SL-based spiral MB (Balun A) with P_2 terminated to a 50 Ω resistor. (b) EM-simulated and RF-measured S-parameters (top) of two resistively terminated MBs (Balun A: P_2 is resistively terminated, Balun B: P_3 is resistively terminated) and calculated EM-simulated and RF-measured AI and PI. The shaded gray area indicates the operational BW.

B. Marchand Baluns

Due to only being able to test the MBs using a two-port GSG characterization system, for each of the two different MBs, two resistively terminated prototypes, named Balun A (P_3 resistively terminated) and Balun B (P_2 resistively

TABLE II
PERFORMANCE COMPARISON WITH SOA MULTILAYER COUPLED-LINE BALUNS

Ref.	f_0 (GHz)	Maximum Loss (dB)	Fractional bandwidth (FBW)			Technology	Volume	
			10 dB RL FBW	Amplitude Imb.	Phase Imb.		mm × mm × mm	$\lambda_g \times \lambda_g \times \lambda_g$
[17]	5.22	2**	120%	<0.8 dB	<5.8°	ML PCB	10.85 × 23.4 × 0.65	0.594 × 1.282 × 0.035
[25]	12	2**	127%	<1 dB	<6°	LCP	/ × / × 0.254	0.5** × 1** × 0.007
[65]	2	0.9	71%**	<0.38 dB	<3.5°	LCP/PCB	18.9 × 48.2 × 1.3	0.20 × 0.50 × 0.14
[66]	2.4	1**	24%	<1 dB	<3°	LTCC	N/A	N/A
[67]	45	7**	89%	<1.5 dB	<10°	CMOS	1 × 0.55 × /	0.296 × 0.163 × /
[68]	2	2**	75%**	N/A	N/A	MMIC	1.3** × 1.3** × /	0.023** × 0.023** × /
[70]	2.6	2.8	31%	<0.5 dB	<5°	ML PCB	33.3 × 50.3 × 0.635	0.51 × 0.77 × 0.01
[75]	1.6	1.3	77%	<1 dB	<10°	LTCC	2 × 1.25 × 0.95	0.101 × 0.063 × 0.048
[76]	4	1*	93%	<0.9 dB	<1.8°	ML PCB	12 × 30.1 × 0.01	0.3 × 0.75 × 0.01
[77]	2.45	0.24	16%	<0.1 dB	<1°	LTCC	2 × 1.2 × 0.8	0.072 × 0.043 × 0.029
[78]	4.45	0.3*	81%	<0.4 dB**	<2.5°	ML PCB	10.1** × 2.43** × 9	0.267** × 0.065** × 0.24
This work (Straight MB)	**4.4**	**3.9#**	**96%**	**<0.9 dB**	**<7°**	**Inkjet AM**	**1.35 × 8.2 × 1.17**	**0.033 × 0.241 × 0.028**
This work (Spiral MB)	**4.4**	**3.1#**	**95%**	**<0.5 dB**	**<7°**	**Inkjet AM**	**1.53 × 3.35 × 1.17**	**0.043 × 0.094 × 0.028**

λ_g: Guided wavelength at f_0; ML: Multilayer; *: Insertion loss at f_0; **: Estimated from graphs/images, /: Measurement not given, #: includes transition loss.

terminated) were manufactured and tested so that each balun is tested as a 2-port device. These separate cases are indicated in the manufactured coupon in Fig. 13(a), with dot-dashed lines indicating the straight baluns, and dashed lines the spiral baluns. An X-ray scan of the coupon is shown in Fig. 13(b).

Beginning with the straight coupled-line case, an X-ray photograph of an example manufactured prototype of the MB is provided in Fig. 14(a). Its EM-simulated and RF-measured performance in terms of S-parameters, AI, and PI is provided in Fig. 14(b). They have been obtained by measuring the S-parameters of two different resistively terminated baluns, namely Balun A and Balun B. The resistive termination was performed with a 50 Ω 0402 resistor. Its RF-measured performance is summarized as follows: center frequency (f_0) = 4.4 GHz, BW between 2.8 and 8 GHz, and FBW of 96.3% that is shaded with a gray area in Fig. 14(b) and appear to be in a good agreement with EM simulations. Across this BW, the measured power loss (where the vertical transition loss is included) was calculated between, 1.2 and 3.9 dB and the PI was 3.5 ± 3.5°, and AI was 0.6 ± 0.3 dB. The finite amount of insertion loss is due to the finite conductivity of the silver ink and the moderate tan(δ) of the dielectric ink. Furthermore, the conductive losses may also be impacted by the finite thickness of the conductors which are about 3× of the skin-depth. Conductive losses may be improved by using thicker conductors and dielectric losses can be minimized by opening air cavities around the TLs, however, at the expense of size. The PI and AI are also plotted in Fig. 14(b) and appear to be slightly higher than the ones predicted in EM simulations. This is due to the AI and PI being calculated by measurements performed between two different prototypes (i.e., Balun A and Balun B) which may be slightly different to one another due to process variations on the same coupon.

To evaluate the manufacturing tolerances effect on the AI and PI of the resistively terminated baluns, the tolerances indicated in Fig. 15(a) are considered. Specifically, all conductive layer thickness can vary within ±1.5 μm, the dielectric layer thickness can vary within ±5%, and the trace width and conductor-to-conductor spacings within ±9 μm. Furthermore, the SMD resistors have a ±10% tolerance. Monte Carlo simulations were performed and are provided in Fig. 15(b). As shown, the obtained AI and PI range overlaps almost fully with the obtained AI and PI responses in RF measurements, demonstrating that it is likely these differences are mostly due to being estimated from two separate, resistively terminated prototypes. The observed PI discrepancies at low frequencies are assumed to be due to the stray capacitances introduced by fabrication errors. However, these are outside of the desired operational range which is quite broad and shows decent AI and PI characteristics. AI and PI naturally are expected to be smaller if measured on a single MB device using 3-port RF characterization.

The spiral MB was also validated experimentally. Its manufactured prototype is provided in Fig. 16(a) and its EM-simulated and RF-measured performance in terms of S-parameters, AI, and PI is provided in Fig. 16(b). They have also been obtained by measuring the S-parameters of two different resistively-terminated baluns. The RF-measured performance is summarized as follows: center frequency (f_0) = 4.4 GHz, BW between 2.8 and 8 GHz, and FBW of 95% that is shaded with a gray area in Fig. 16(b). Across this BW, the power loss (where the slanted vertical transition loss is included) was measured between 1.2 and 3.9 dB, the PI was 3.5 ± 3.5°, and the AI was 0.6 ± 0.3 dB. The EM simulation responses are also provided and are in good agreement with the EM-simulated ones successfully validating the proposed spiral MB balun concept.

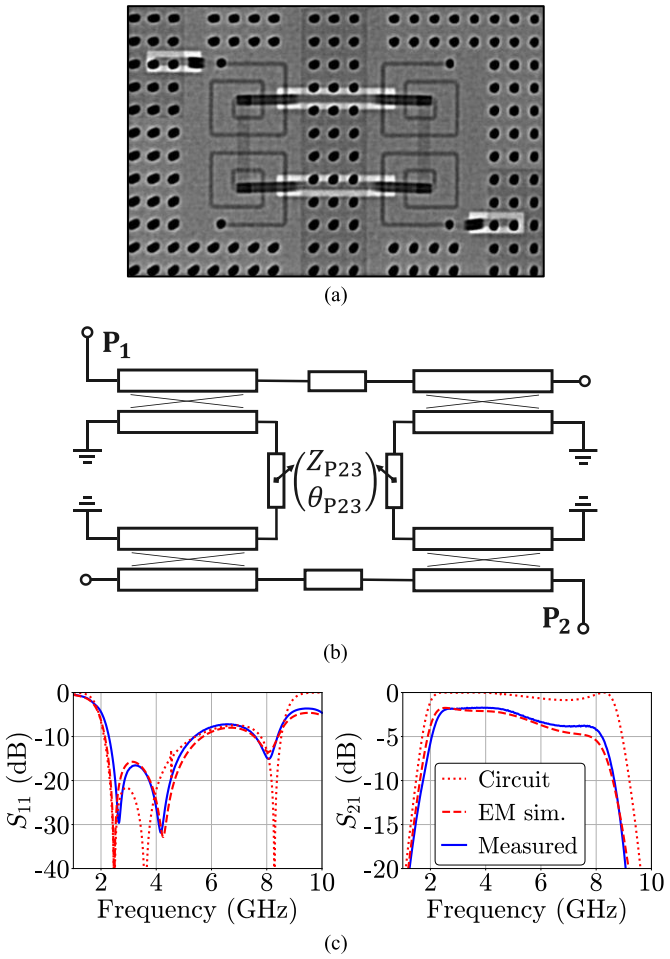

Fig. 17. Characterization of the spiral SL-based MB in a back-to-back configuration. (a) X-ray image of the prototype. (b) Illustrative circuit schematic, indicating the additional lines required to connect the two spiral baluns in a back-to-back configuration where $Z_{P23} = 50\ \Omega, \theta_{P23} = 15°$. (c) Circuit-simulated, EM-simulated, and RF-measured S-parameters.

The spiral MB performance was also evaluated by manufacturing and testing an additional prototype with two MBs arranged in a back-to-back configuration. TLs were required to route signals out from the center of each spiral. Its photograph, illustrative circuit schematic, and EM-simulated and RF-measured responses are provided in Fig. 17. The RF-measured performance is seen to be in a close agreement with the EM-simulated one, successfully validating the proposed concept. It exhibits an insertion loss of 1.8 dB at $f_0 = 4.4$ GHz, with a 3 dB BW from 2.1 to 8.1 GHz.

Table II compares the proposed inkjet-printed MBs with other state-of-the-art (SOA) coupled-line baluns realized with multilayer processes, e.g. LTCC, MMIC, CMOS, and multilayer PCB (ML PCB). As shown, the proposed MB configurations exhibit small physical size, especially in the spiral case, and competitive RF performance. In particular, for the spiral balun, it shows comparable AI and PI with most of the presented approaches (e.g., in [65] and [70]) and in some occasions, its AI, PI, and size are smaller than the SOA (e.g., its AI is smaller than in [17], [26], [66], [67], [75], and [76], its PI is smaller than in [67] and [75], and its size is smaller than in [17], [26], [36], [65], [67], [70], [75], and [78]) while excluding [17], [26], it exhibits the widest FBW, which is very close to the optimally predicted 99% by the theoretical analysis in Section II-A. Although its loss may appear to be higher than certain integration concepts (e.g., LTCC [66], [75], [77], CMOS [67]), to the best of the authors' knowledge, this is the first time that a wideband MB has been implemented monolithically using a two-material inkjet printing process, which demonstrates comparable or even better performance (in terms of FBW) than SOA multilayer processes. Processes that are potentially more expensive require expensive cleanroom manufacturing facilities and do not facilitate such levels of design flexibility.

IV. Conclusion

This manuscript presented a detailed design methodology for the practical development of wideband MBs, alongside a unique integration concept using multimaterial inkjet printing. An optimization method determining the maximum achievable FBW for alternative RF input/output impedances was proposed for the first time. Several TL-based integration concepts were analyzed using 2-D and 3-D EM simulations taking into consideration the capabilities of a multimaterial multilayer inkjet printing process which is used in this work for the realization of MBs for first time. A miniaturization scheme using spiral TLs and slanted vias was also explored for size compactness. To validate this approach, the properties of the inkjet printing process were evaluated through test structures, optical characterization methods and RF testing. Lastly, several coupled-line test structures and MBs were designed, manufactured, and tested in resistively terminated and back-to-back configurations.

Acknowledgment

The authors would like to thank Nano Dimension for their guidance in the process specifics and for manufacturing the prototypes. They would also like to thank Finbarr Waldon at Tyndall National Institute for assisting with the optical characterization.

References

[1] A. Munk, J. Kraus, and R. Marhefka, *Antennas for All Applications*, 3rd ed. New York, NY, USA: McGraw-Hill, 2002.

[2] T. H. Chen et al., "Broadband monolithic passive baluns and monolithic double-balanced mixer," in *IEEE MTT-S Int. Microw. Symp. Dig.*, Dec. 1991, vol. 2, no. 12, pp. 861–864, doi: 10.1109/MWSYM.1991.147143.

[3] P.-C. Hsu, C. Nguyen, and M. Kintis, "Uniplanar broad-band push-pull FET amplifiers," *IEEE Trans. Microw. Theory Techn.*, vol. 45, no. 12, pp. 2150–2152, Dec. 1997.

[4] S. Maas and Y. Ryu, "A broadband, planar, monolithic resistive frequency doubler," in *IEEE Int. Microw. Symp. Dig.*, May 1994, pp. 443–446.

[5] F. Aryanfar and C. Werner, "An amplitude-based phase detector at MM-wave frequency range," in *IEEE MTT-S Int. Microw. Symp. Dig.*, Jun. 2011, pp. 1–4, doi: 10.1109/MWSYM.2011.5972986.

[6] P.-H. Tsai, Y.-H. Lin, J.-L. Kuo, Z.-M. Tsai, and H. Wang, "Broadband balanced frequency doublers with fundamental rejection enhancement using a novel compensated Marchand balun," *IEEE Trans. Microw. Theory Techn.*, vol. 61, no. 5, pp. 1913–1923, May 2013.

[7] C. Liu and W. Menzel, "Broadband via-free microstrip balun using metamaterial transmission lines," *IEEE Microw. Wireless Compon. Lett.*, vol. 18, no. 7, pp. 437–439, Jul. 2008, doi: 10.1109/LMWC.2008.924913.

[8] I. S. Krishna and S. Mukherjee, "Design of folded substrate integrated coaxial line wideband balun for K-band applications," in *Proc. IEEE Indian Conf. Antennas Propogation (InCAP)*, Dec. 2018, pp. 1–4, doi: 10.1109/INCAP.2018.8770732.

[9] J. Shao, R. Zhou, C. Chen, X.-H. Wang, H. Kim, and H. Zhang, "Design of a wideband balun using parallel strips," *IEEE Microw. Wireless Compon. Lett.*, vol. 23, no. 3, pp. 125–127, Mar. 2013, doi: 10.1109/LMWC.2013.2246150.

[10] Y.-Q. Yu, W. Jiang, L. Qin, H.-Y. Shao, and S.-X. Gong, "Design of a planar transmission line balun based on novel phase inverter," *IEEE Access*, vol. 8, pp. 18915–18924, 2020, doi: 10.1109/ACCESS.2020.2968341.

[11] M. S. Mahani and R. Abhari, "A planar ultra wide band single layer microstrip BALUN operating from 200 MHz to 10 GHz," in *IEEE MTT-S Int. Microw. Symp. Dig.*, Jun. 2012, pp. 1–3, doi: 10.1109/MWSYM.2012.6259713.

[12] J.-S. Lim et al., "800–5000 MHz ultra-wideband CPW balun," *Electron. Lett.*, vol. 42, no. 18, pp. 1037–1039, 2006, doi: 10.1049/el:20061448.

[13] C.-H. Tseng and C.-L. Chang, "Wide-band balun using composite right/left-handed transmission line," *Electron. Lett.*, vol. 41, no. 2, pp. 40–41, 2005, doi: 10.1049/el:20071759.

[14] M. A. Antoniades and G. V. Eleftheriades, "A broadband Wilkinson balun using microstrip metamaterial lines," *IEEE Antennas Wireless Propag. Lett.*, vol. 4, pp. 209–212, 2005.

[15] Z.-Y. Zhang, Y.-X. Guo, L. C. Ong, and M. Y. W. Chia, "A new wide-band planar balun on a single-layer PCB," *IEEE Microw. Wireless Compon. Lett.*, vol. 15, no. 6, pp. 416–418, Jun. 2005, doi: 10.1109/LMWC.2005.850486.

[16] S. Guan, X. Bi, Q. Ma, and Q. Xu, "A wideband balun filter based on folded ring slotline resonator and dual-feedback stubs with >17.8 f_0 stopband rejection," *IEEE Trans. Circuits Syst. II, Exp. Briefs*, vol. 70, no. 2, pp. 466–470, Feb. 2023, doi: 10.1109/TCSII.2022.3174954.

[17] L.-P. Feng and L. Zhu, "Wideband filtering balun on a novel hybrid multimode resonator with the functionality of vertical transition," *IEEE Trans. Compon., Packag., Manuf. Technol.*, vol. 7, no. 8, pp. 1324–1330, Aug. 2017, doi: 10.1109/TCPMT.2017.2658669.

[18] Z. Feng, X. Bi, Z. Cao, A. Shen, Q. Ding, and Q. Xu, "A filtering balun utilizing multi-ring loaded vertical transition structure with 161% fractional bandwidth and >5.8 f_0 stopband," *IEEE Trans. Circuits Syst. II, Exp. Briefs*, vol. 69, no. 4, pp. 2061–2065, Apr. 2022, doi: 10.1109/TCSII.2021.3139158.

[19] A. K. Poddar, U. L. Rohde, V. Madhavan, and S. K. Koul, "A novel UWB balun: Application in 5G systems," in *Proc. IEEE Int. Freq. Control Symp. (IFCS)*, May 2016, pp. 1–7, doi: 10.1109/FCS.2016.7546747.

[20] Z. Chi, Y. Rao, Z. Deng, C. Han, and X. Luo, "Wideband filtering balun with wide stopband and imbalance compensation using hybrid DGS with float strip-line," in *Proc. IEEE Int. Symp. Radio-Frequency Integr. Technol. (RFIT)*, Aug. 2021, pp. 1–3, doi: 10.1109/RFIT52905.2021.9565284.

[21] L. Yang, L. Zhu, W.-W. Choi, K.-W. Tam, R. Q. Zhang, and J. P. Wang, "Wideband balanced-to-unbalanced bandpass filters synthetically designed with Chebyshev filtering response," *IEEE Trans. Microw. Theory Techn.*, vol. 66, no. 10, pp. 4528–4539, Oct. 2018.

[22] N. Marchand, "Transmission line conversion transformers," *Electronics*, vol. 17, pp. 142–145, Dec. 1944.

[23] R. Bawer and J. J. Wolfe, "A printed circuit balun for use with spiral antennas," *IRE Trans. Microw. Theory Techn.*, vol. 8, no. 3, pp. 319–325, May 1960.

[24] K.-C. Lin and Y.-C. Lin, "A simple printed compensated balun for enhanced ultra-wideband performances," *IEEE Microw. Wireless Compon. Lett.*, vol. 24, no. 1, pp. 5–7, Jan. 2014, doi: 10.1109/LMWC.2013.2285211.

[25] A. C. Chen, A.-V. Pham, and R. E. Leoni, "Development of low-loss broad-band planar baluns using multilayered organic thin films," *IEEE Trans. Microw. Theory Techn.*, vol. 53, no. 11, pp. 3648–3655, Nov. 2005.

[26] A. C. Chen, A.-V. Pham, and R. E. Leoni III, "A novel broadband even-mode matching network for Marchand baluns," *IEEE Trans. Microw. Theory Techn.*, vol. 57, no. 12, pp. 2973–2980, Dec. 2009.

[27] X. Lan et al., "An ultra-wideband balun using multi-metal GaAs MMIC technology," *IEEE Microw. Wireless Compon. Lett.*, vol. 20, no. 8, pp. 474–476, Aug. 2010.

[28] Z. Zhang, Y.-X. Guo, L. C. Ong, and M. Y. W. Chia, "Improved planar Marchand balun using a patterned ground plane," *Int. J. RF Microw. Comput.-Aided Eng.*, vol. 15, no. 3, pp. 307–316, 2005, doi: 10.1002/mmce.20084.

[29] M. J. Chiang, H. S. Wu, and C. K. C. Tzuang, "A compact CMOS Marchand balun incorporating meandered multilayer edge-coupled transmission lines," in *Proc. IEEE Int. Microw. Symp.*, Jun. 2009, pp. 125–128, doi: 10.1109/MWSYM.2009.5165648.

[30] H.-W. Chin, L.-T. Hwang, F.-S. Chang, S.-M. Wang, and P.-S. Li, "Design of an IPD ultra wideband Marchand balun using a phase compensation line," in *Proc. Asia–Pacific Microw. Conf. (APMC)*, vol. 2, Dec. 2015, pp. 1–3.

[31] K. Nishikawa, I. Toyoda, and T. Tokumitsu, "Compact and broad-band three-dimensional MMIC balun," *IEEE Trans. Microw. Theory Techn.*, vol. 47, no. 1, pp. 96–98, Jan. 1999.

[32] S. Chakraborty, L. E. Milner, X. Zhu, O. Sevimli, A. E. Parker, and M. C. Heimlich, "An edge-coupled Marchand balun with partial ground for excellent balance in 0.13 μm SiGe technology," *IEEE Trans. Circuits Syst. II, Exp. Briefs*, vol. 68, no. 1, pp. 226–230, Jan. 2021, doi: 10.1109/TCSII.2020.3004642.

[33] W. M. Fathelbab and M. B. Steer, "New classes of miniaturized planar Marchand baluns," *IEEE Trans. Microw. Theory Techn.*, vol. 53, no. 4, pp. 1211–1220, Apr. 2005.

[34] M. Johnston, C. Van Niekerk, and D. I. L. de Villiers, "Ultra-wideband planar Marchand balun design for the pyramidal sinuous antenna," in *Proc. IEEE Int. Symp. Antennas Propag. USNC-URSI Radio Sci. Meeting*, Jul. 2019, pp. 735–736.

[35] R. Phromloungsri, M. Chongcheawchamnan, and I. D. Robertson, "Inductively compensated parallel coupled microstrip lines and their applications," *IEEE Trans. Microw. Theory Techn.*, vol. 54, no. 9, pp. 3571–3582, Sep. 2006.

[36] C.-H. Tseng and Y.-C. Hsiao, "A new broadband Marchand balun using slot-coupled microstrip lines," *IEEE Microw. Wireless Compon. Lett.*, vol. 20, no. 3, pp. 157–159, Mar. 2010.

[37] G. Yang, Z. Wang, Z. Li, Q. Li, and F. Liu, "Balance-compensated asymmetric Marchand baluns on silicon for MMICs," *IEEE Microw. Wireless Compon. Lett.*, vol. 24, no. 6, pp. 391–393, Jun. 2014.

[38] V. M. Pepino, A. F. da Mota, A. Martins, and B. V. Borges, "3-D-printed dielectric metasurfaces for antenna gain improvement in the Ka-band," *IEEE Antennas Wireless Propag. Lett.*, vol. 17, pp. 2133–2136, 2018, doi: 10.1109/LAWP.2018.2860521.

[39] S. Wang, X. Zhang, L. Zhu, and W. Wu, "Single-fed wide-beamwidth circularly polarized patch antenna using dual-function 3-D printed substrate," *IEEE Antennas Wireless Propag. Lett.*, vol. 17, pp. 649–653, 2018, doi: 10.1109/LAWP.2018.2810105.

[40] S. Alkaraki, Y. Gao, S. Stremsdoerfer, E. Gayets, and C. G. Parini, "3D printed corrugated plate antennas with high aperture efficiency and high gain at X-band and Ka-band," *IEEE Access*, vol. 8, pp. 30643–30654, 2020, doi: 10.1109/ACCESS.2020.2972101.

[41] K. Johnson et al., "Digital manufacturing of pathologically-complex 3D printed antennas," *IEEE Access*, vol. 7, pp. 39378–39389, 2019, doi: 10.1109/ACCESS.2019.2906868.

[42] V. T. Bharambe, J. Ma, M. D. Dickey, and J. J. Adams, "Planar, multifunctional 3D printed antennas using liquid metal parasitics," *IEEE Access*, vol. 7, pp. 134245–134255, 2019, doi: 10.1109/ACCESS.2019.2942058.

[43] S. Sarjoghian, M. H. Sagor, Y. Alfadhl, and X. Chen, "A 3D-printed high-dielectric filled elliptical double-ridged horn antenna for biomedical monitoring applications," *IEEE Access*, vol. 7, pp. 94977–94985, 2019, doi: 10.1109/ACCESS.2019.2928629.

[44] B. Li, P. F. Jing, L. Q. Sun, K. W. Leung, and X. Lv, "3D printed OAM reflectarray using half-wavelength rectangular dielectric element," *IEEE Access*, vol. 8, pp. 142892–142899, 2020, doi: 10.1109/ACCESS.2020.3013678.

[45] B. Sanz-Izquierdo and E. A. Parker, "3-D printing of elements in frequency selective arrays," *IEEE Trans. Antennas Propag.*, vol. 62, no. 12, pp. 6060–6066, Dec. 2014, doi: 10.1109/TAP.2014.2359470.

[46] A. Vallecchi, D. Cadman, W. G. Whittow, J. Vardaxoglou, E. Shamonina, and C. J. Stevens, "3-D printed bandpass filters with coupled vertically extruded split ring resonators," *IEEE Trans. Microwave Theory Techn.*, vol. 67, no. 11, pp. 4341–4352, Nov. 2019, doi: 10.1109/TMTT.2019.2934456.

[47] G. Lipkowitz et al., "Injection continuous liquid interface production of 3D objects," *Sci. Adv.*, vol. 8, no. 39, pp. 1349–1352, Sep. 2022, doi: 10.1126/sciadv.abq3917.

[48] J. P. Kruth, X. Wang, T. Laoui, and L. Froyen, "Lasers and materials in selective laser sintering," *Assem. Autom.*, vol. 23, no. 4, pp. 357–371, Dec. 2003.

[49] P. M. Njogu et al., "Evaluation of planar inkjet-printed antennas on a low-cost origami flapping robot," *IEEE Access*, vol. 8, pp. 164103–164113, 2020, doi: 10.1109/ACCESS.2020.3020824.
[50] S. Jun et al., "Circular polarised antenna fabricated with low-cost 3D and inkjet printing equipment," *Electron. Lett.*, vol. 53, no. 6, pp. 370–371, Mar. 2017, doi: 10.1049/el.2016.4605.
[51] A. Chauraya et al., "Inkjet printed dipole antennas on textiles for wearable communications," *IET Microw., Antennas Propag.*, vol. 7, no. 9, pp. 760–767, Jun. 2013, doi: 10.1049/iet-map.2013.0076.
[52] B. S. Cook and A. Shamim, "Inkjet printing of novel wideband and high gain antennas on low-cost paper substrate," *IEEE Trans. Antennas Propag.*, vol. 60, no. 9, pp. 4148–4156, Sep. 2012, doi: 10.1109/TAP.2012.2207079.
[53] G. McKerricher, D. Titterington, and A. Shamim, "A fully inkjet-printed 3-D honeycomb-inspired patch antenna," *IEEE Antennas Wireless Propag. Lett.*, vol. 15, pp. 544–547, 2016, doi: 10.1109/LAWP.2015.2457492.
[54] B. K. Tehrani, B. S. Cook, and M. M. Tentzeris, "Inkjet printing of multilayer millimeter-wave yagi-uda antennas on flexible substrates," *IEEE Antennas Wireless Propag. Lett.*, vol. 15, pp. 143–146, 2016.
[55] A. Shastri et al., "3D printing of millimetre wave and low-terahertz frequency selective surfaces using aerosol jet technology," *IEEE Access*, vol. 8, pp. 177341–177350, 2020.
[56] Nano Dimension. *The Material Advantage of DragonFlyTM*. Accessed: Jan. 15, 2024. [Online]. Available: https://www.nano-di.com/ame-materials
[57] J. Zhu et al., "Additively manufactured millimeter-wave dual-band single-polarization shared aperture Fresnel zone plate metalens antenna," *IEEE Trans. Antennas Propag.*, vol. 69, no. 10, pp. 6261–6272, Oct. 2021, doi: 10.1109/TAP.2021.3070224.
[58] M. Li, Y. Yang, F. Iacopi, J. Nulman, and S. Chappel-Ram, "3D-printed low-profile single-substrate multi-metal layer antennas and array with bandwidth enhancement," *IEEE Access*, vol. 8, pp. 217370–217379, 2020.
[59] J. Zhu, Y. Yang, J. Lai, and J. Nulman, "Additively manufactured polarization insensitive broadband transmissive metasurfaces for arbitrary polarization conversion and wavefront shaping," *Adv. Opt. Mater.*, vol. 10, no. 21, pp. 1–12, Nov. 2022, doi: 10.1002/adom.202200928.
[60] J. Zhu, M. Li, J. Lai, and Y. Yang, "Multimaterial additively manufactured transmissive spin-decoupled polarization-maintaining metasurfaces," *Laser Photon. Rev.*, vol. 17, no. 12, pp. 1–13, Dec. 2023, doi: 10.1002/lpor.202300433.
[61] J. Zhu, Y. Yang, N. Hu, S. Liao, and J. Nulman, "Additively manufactured multi-material ultrathin metasurfaces for broadband circular polarization decoupled beams and orbital angular momentum generation," *ACS Appl. Mater. Interfaces*, vol. 13, no. 49, pp. 59460–59470, Dec. 2021, doi: 10.1021/acsami.1c16493.
[62] M. Li, Y. Yang, F. Iacopi, M. Yamada, and J. Nulman, "Compact multilayer bandpass filter using low-temperature additively manufacturing solution," *IEEE Trans. Electron Devices*, vol. 68, no. 7, pp. 3163–3169, Jul. 2021, doi: 10.1109/TED.2021.3072926.
[63] M. Li, Y. Yang, Y. Zhang, F. Iacopi, S. Ram, and J. Nulman, "A fully integrated conductive and dielectric additive manufacturing technology for microwave circuits and antennas," in *Proc. 50th Eur. Microw. Conf. EuMC*, 2020, 2021, pp. 392–395, doi: 10.23919/EuMC48046.2021.9338141.
[64] Keysight Technologies. (2021). *Advanced Design System (ADS)*. [Online]. Available: https://www.keysight.com/en/pd-1000000716%3Aepsg%3Apro-pn-ADS
[65] F. Huang, J. Wang, K. Aliqab, J. Hong, and W. Wu, "Analysis and design of a new self-packaged wideband balun bandpass filter with the functionality of impedance transformation," *IEEE Trans. Microw. Theory Techn.*, vol. 67, no. 6, pp. 2322–2330, Jun. 2019.
[66] Y.-X. Guo, Z.-Y. Zhang, L. C. Ong, and M. Y. W. Chia, "Design of miniaturized LTCC baluns," *Int. J. RF Microw. Comput.-Aided Eng.*, vol. 16, no. 3, pp. 268–279, 2006, doi: 10.1002/mmce.20151.
[67] C. Liu, C. Hsu, H. Chuang, and C. Chen, "A 60-GHz millimeter-wave CMOS Marchand balun using 0.18-μm CMOS technology," *Microw. Opt. Technol. Lett.*, vol. 51, no. 3, pp. 766–770, Mar. 2009, doi: 10.1002/mop.24176.
[68] R. H. Jansen, J. Jotzo, and R. Engels, "Improved compaction of multilayer MMIC/MCM baluns using lumped element compensation," in *IEEE MTT-S Int. Microw. Symp. Dig.*, vol. 1, Jun. 1997, pp. 277–280.
[69] M. C. Tsai, "A new compact wideband balun," in *IEEE MTT-S Int. Microw. Symp. Dig.*, Jun. 1993, pp. 141–143.
[70] S. Lin, J. Wang, G. Zhang, and J. Hong, "Design of microstrip tri-mode balun bandpass filter with high selectivity," *Electron. Lett.*, vol. 51, no. 13, pp. 998–999, Jun. 2015, doi: 10.1049/el.2015.1047.
[71] D. Sokol, M. Yamada, and J. Nulman, "Design and performance of additively manufactured in-circuit board planar capacitors," *IEEE Trans. Electron Devices*, vol. 68, no. 11, pp. 5747–5752, Nov. 2021, doi: 10.1109/TED.2021.3117934.
[72] Ansys. *High-Frequency Structure Simulator (HFSS)*. Accessed: Jan. 15, 2024. [Online]. Available: https://www.ansys.com/products/electronics/ansys-hfss
[73] I. J. Bahl and P. Bhartia, "Characteristics of inhomogeneous broadside-coupled striplines," *IEEE Trans. Microw. Theory Techn.*, vol. MTT-28, no. 6, pp. 529–535, Jun. 1980.
[74] S.-M. Wang, C.-H. Chi, M.-Y. Hsieh, and C.-Y. Chang, "Miniaturized spurious passband suppression microstrip filter using meandered parallel coupled lines," *IEEE Trans. Microw. Theory Techn.*, vol. 53, no. 2, pp. 747–753, Feb. 2005.
[75] Y. Dai, H. Yin, Y. Feng, P. Li, Q. Han, and M. Han, "A LTCC miniaturized broadband modified Marchand balun," in *Proc. Int. Symp. Commun. Inf. Technol. (ISCIT)*, Oct. 2012, pp. 110–113, doi: 10.1109/ISCIT.2012.6380858.
[76] F. Huang, J. Wang, J. Hong, and W. Wu, "Wideband balun bandpass filter with broadside-coupled microstrip/slotline resonator structure," *Electron. Lett.*, vol. 53, no. 19, pp. 1320–1321, Sep. 2017, doi: 10.1049/el.2017.2835.
[77] C.-W. Tang and C.-Y. Chang, "A semi-lumped balun fabricated by low temperature co-fired ceramic," in *IEEE MTT-S Int. Microw. Symp. Dig.*, Jun. 2002, pp. 2201–2204, doi: 10.1109/MWSYM.2002.1012309.
[78] Y. Wang, K. Ma, and M. Yu, "A low-cost substrate integrated suspended line platform with multiple inner boards and its applications in coupled-line circuits," *IEEE Trans. Compon., Packag., Manuf. Technol.*, vol. 10, no. 12, pp. 2087–2098, Dec. 2020, doi: 10.1109/TCPMT.2020.3032296.
[79] D. E. Bockelman and W. R. Eisenstadt, "Pure-mode network analyzer for on-wafer measurements of mixed-mode S-parameters of differential circuits," *IEEE Trans. Microw. Theory Techn.*, vol. MTT-45, no. 7, pp. 1071–1077, Jul. 1997.

Joe Steele received the bachelor's degree (Hons.) in applied mathematics and physics from University College Cork, Cork, Ireland, in 2022, where he is currently pursuing the master's degree in RF/microwave engineering.

His main research interests include wideband baluns, multilayer design, and additively manufactured electronics.

Dimitra Psychogiou (Senior Member, IEEE) received the Dipl.-Eng. degree in electrical and computer engineering from the University of Patras, Patras, Greece, in 2008, and the Ph.D. degree in electrical engineering from Swiss Federal Institute of Technology (ETH), Zürich, Switzerland, in 2013.

She is currently a Professor of electrical and electronic engineering at the University College Cork (UCC), Cork, Ireland, and the Head of the Advanced RF Technology Group at Tyndall National Institute, Cork. Prior to joining UCC, she was a Sr. Research Scientist at Purdue University, West Lafayette, IN, USA, and an Assistant Professor at the University of Colorado Boulder, Boulder, CO, USA. Her current research interests include RF design and characterization of reconfigurable microwave and millimeter-wave passive components, RF-MEMS, acoustic wave resonator-based filters, tunable filter synthesis, frequency-agile antennas, and additive manufacturing technologies for 3-D antenna sub-systems. Her research has been presented in more than 250 publications and has received the 2023 IEEE MTT-S Outstanding Young Engineer Award, the 2021 Roberto Sorrentino Prize, the SFI Research Professorship Award, the 2020 NSF CAREER Award the 2020 URSI Young Scientist Award, and the Junior Faculty Outstanding Research Award from UC Boulder. Her students have also received numerous student-paper awards and research-based fellowships.

Prof. Psychogiou is a Senior Member of IEEE and URSI and a member of the IEEE MTT-S Filters and Passive Components (MTT-5) and Microwave Control Materials and Devices (MTT-13) committees. She is currently serving as the President of URSI Ireland, the Vic-Chair of MTT-13 and the Secretary of USNC-URSI Commission D. She is also an Associate Editor of IEEE MICROWAVE AND WIRELESS COMPONENTS LETTERS and the *International Journal of Microwave and Wireless Technologies* and is on the Technical Review Board of various IEEE and EuMA conferences. Previously, she was an Associate Editor of the *IET Microwaves, Antennas and Propagation Journal*.